

UniManip: General-Purpose Zero-Shot Robotic Manipulation with Agentic Operational Graph

Haichao Liu, Yuanjiang Xue, Yuheng Zhou, Haoyuan Deng, Yinan Liang, Lihua Xie, and Ziwei Wang

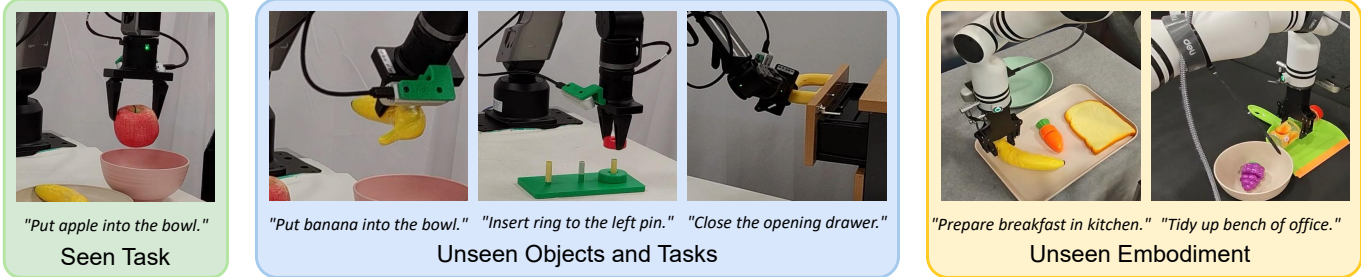


Fig. 1: UniManip achieves robust, general-purpose robotic manipulation in open-world settings. The system supports zero-shot transfer across diverse embodiments (fixed and mobile) and utilizes a graph-based agentic workflow to adapt to errors during long-horizon tasks, ensuring high success rates without reconfiguration.

Abstract—Achieving general-purpose robotic manipulation requires robots to seamlessly bridge high-level semantic intent with low-level physical interaction in unstructured environments. However, existing approaches falter in zero-shot generalization: end-to-end Vision-Language-Action (VLA) models often lack the precision required for long-horizon tasks, while traditional hierarchical planners suffer from semantic rigidity when facing open-world variations. To address this, we present UniManip, a framework grounded in a Bi-level Agentic Operational Graph (AOG) that unifies semantic reasoning and physical grounding. By coupling a high-level Agentic Layer for task orchestration with a low-level Scene Layer for dynamic state representation, the system continuously aligns abstract planning with geometric constraints, enabling robust zero-shot execution. Unlike static pipelines, UniManip operates as a dynamic agentic loop: it actively instantiates object-centric scene graphs from unstructured perception, parameterizes these representations into collision-free trajectories via a safety-aware local planner, and exploits structured memory to autonomously diagnose and recover from execution failures. Extensive experiments validate the system’s robust zero-shot capability on unseen objects and tasks, demonstrating a 22.5% and 25.0% higher success rate compared to state-of-the-art VLA and hierarchical baselines, respectively. Notably, the system enables direct zero-shot transfer from fixed-base setups to mobile manipulation without finetuning or reconfiguration. Our open-source project page can be found at <https://henryhcliu.github.io/unimanip>.

Index Terms—Robotic manipulation, bi-level agentic operational graph, zero-shot, long-horizon, failure recovery

I. INTRODUCTION

General-purpose robotic manipulation aims to deploy agents into unstructured, open-world environments where they must

Haichao Liu, Yuanjiang Xue, Yuheng Zhou, Haoyuan Deng, Lihua Xie, and Ziwei Wang are with the School of Electrical and Electronic Engineering, Nanyang Technological University, Singapore (e-mail: haichao.liu@ntu.edu.sg; e250086@e.ntu.edu.sg; yuheng.zhou@ntu.edu.sg; haoyuan.deng@ntu.edu.sg; elhxie@ntu.edu.sg; ziwei.wang@ntu.edu.sg).

Yinan Liang is with the Department of Automation, Tsinghua University, China (email: liangyn24@mails.tsinghua.edu.cn)

This work has been submitted to the IEEE for possible publication. Copyright may be transferred without notice, after which this version may no longer be accessible.

execute diverse tasks without pre-configuration. Central to this utility is zero-shot generalization, the capacity to instantly adapt to novel objects and layouts without task-specific training or fine-tuning [1], [2]. However, replicating human-level adaptability remains a formidable challenge due to the fundamental disconnect between learned priors and novel realities. The primary bottleneck in current systems is the out-of-distribution (OOD) condition: end-to-end models often fail when facing unseen visual data or free-form human commands that deviate from training distributions, whereas traditional hierarchical planners lack the semantic flexibility to handle unexpected faults. Consequently, achieving robust zero-shot performance demands more than open-loop execution; it requires a fundamental reasoning ability, specifically, an agentic capacity to continuously perceive, verify, and autonomously reflect to realign high-level intent with the unscripted physical world [3], [4].

To approach zero-shot generalization, current research predominantly follows two paradigms: data-driven Vision-Language-Action (VLA) adaptation [5]–[9] and structured hierarchical planning [10]–[15]. In the VLA domain, strategies like in-context learning [16], [17] and parameter-efficient finetuning [18] attempt to steer frozen priors toward new tasks. However, these methods remain fundamentally bounded by their backbone’s training distribution, struggling to generalize to unseen kinematics or out-of-distribution dynamics without high-quality demonstrations. Conversely, hierarchical frameworks [10]–[15] leverage VLMs or PDDL to decompose tasks into symbolic plans, yet they typically treat planning and execution as isolated stages. This separation results in brittleness, as high-level logic lacks the dynamic physical grounding and closed-loop feedback required to adapt when primitives fail [10]. This dilemma leads to a critical research question: *How can we efficiently represent scenario conditions and spatial operations to serve VLM reasoning while seamlessly bridging it with precise, low-level manipulation execution?*

To bridge this divide, we propose UniManip, a general-

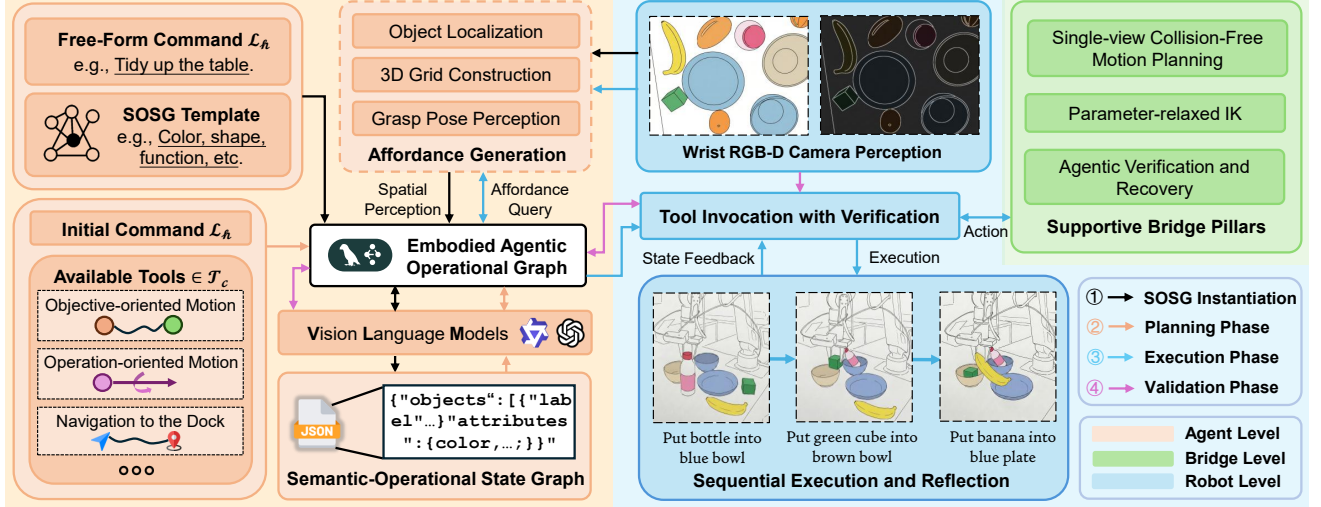


Fig. 2: Overview of the UniManip framework. The system integrates high-level task planning with low-level motion execution through an Agentic Operational Graph (AOG), illustrated at the agent level. The VLM interprets human commands to generate an operational graph, which guides the robot’s actions. A reflective recovery mechanism allows the system to diagnose and adapt to execution failures.

purpose framework founded on a novel Bi-level Agentic Operational Graph (AOG) that mimics the cognitive interplay of human memory systems [19]. Unlike conventional hierarchical methods that rigidly separate planning from execution, UniManip unifies them through two interacting layers grounded in distinct cognitive functions. The upper *agentic logic layer* functions as the system’s procedural and semantic memory: it governs high-level reasoning, orchestrates task flow, verifies outcomes, and manages recovery from partial failures, effectively acting as the “prefrontal cortex” of the agent. Conversely, the lower *semantic-operational state layer* serves as the dynamic episodic memory: it maintains an adaptive, grounded representation of object states and spatial affordances. By explicitly coupling these memory systems, the AOG enables the agent to not only plan actions but to actively update its understanding of the physical world, ensuring that high-level logic remains continuously synchronized with low-level reality.

As illustrated in Fig. 2, this agentic framework operates through three logically connected phases: First, multimodal scene instantiation, which instantiates multimodal inputs into object-centric geometric attributes and physical affordances. Second, agentic primitive execution, which generates skill primitives and drives action parameterization via a single-view conservative reconstruction approach, utilizing safety-aware objectives to ensure collision-free trajectories. Third, closed-loop reflection and recovery, which exploits the AOG’s structured memory to autonomously diagnose execution anomalies and dynamically restructure the logic graph for recovery.

The main contributions are summarized as follows:

- We propose UniManip, a general-purpose manipulation framework that achieves robust zero-shot generalization across diverse tasks, objects, and robot embodiments without task-specific fine-tuning or reconfiguration.
- We introduce the Bi-level AOG, which serves as an agentic infrastructure. By implicitly integrating semantic and episodic memory, the AOG enables sophisticated

reasoning and dynamic task decomposition while maintaining synchronization with the physical environment.

- We establish a robust task-to-motion bridge that combines single-view conservative reconstruction with a safety-aware planner, enabling the generation of optimized, collision-free, and efficient end-effector trajectories.
- We demonstrate that UniManip outperforms SOTA VLA and hierarchical baselines by 22.5% and 25.0%, respectively, while validating its versatility through zero-shot transfer to mobile manipulation in unseen environments.

II. RELATED WORK

We review related work in the following areas: End-to-end methods without reasoning, hierarchical methods with the paradigm of planning before action, and failure detection and recovery in robotic manipulation.

A. VLA Models for Manipulation

This category of methods maps raw sensory observations directly to low-level robot actions, leveraging the scaling laws of large imitation learning datasets [20]. Representative examples include RT-1 [21], PaLM-E [22], OpenVLA [6], π_0 [7], and GR0OT [23]. These models typically fuse visual and textual inputs within a unified transformer architecture to generate motor commands. Beyond fully offline training, recent work has explored few-shot adaptation of pretrained VLAs to new tasks. MoS-VLA [16] demonstrates one-shot skill adaptation, while *Learning a thousand tasks in a day* [17] scales rapid task acquisition through large-scale multi-task learning and transfer. ControlVLA [18] further improves few-shot generalization via object-centric adaptation of pretrained VLA backbones. Moreover, Nora 1.5 [8] leverages reward-guided post-training to achieve high-fidelity zero-shot performance across unseen tasks and object categories.

Despite strong performance in seen or lightly adapted settings, these methods often behave as “black boxes” with

limited explicit state grounding and minimal built-in mechanisms for long-horizon verification and recovery [24], making them sensitive to distribution shifts and difficult to interpret.

B. Hierarchical Methods with Planning before Action

To compensate for the limited explicit reasoning in end-to-end VLAs, recent work decouples high-level planning from low-level execution. These approaches can be broadly divided into sub-task guided VLA models [25]–[28] and hierarchical reasoning-control frameworks [10]–[13], [29]–[32].

Sub-task guided VLA models introduce an explicit planning or reasoning stage before producing actions (often via an action tokenizer). For instance, $\pi_{0.5}$ [25] uses a pretrained VLM to generate sub-tasks that are subsequently executed by a fine-tuned VLA. CoT-VLA [26] incorporates a visual chain-of-thought mechanism by autoregressively predicting future frames as visual goals that guide short-horizon action generation. Similarly, ECoT [27] trains VLAs to perform multi-step reasoning over plans, sub-tasks, and grounded intermediates (e.g., object bounding boxes) before predicting robot actions. GigaBrain-0 [28] emphasizes language-based subgoal generation and jointly optimizes trajectory regression, subgoals, and discrete action tokens. Despite improved interpretability at the planning stage, these methods are often data-hungry and can remain brittle under OOD conditions.

Methods that bridge high-level reasoning with low-level geometric control typically introduce structured intermediate representations (e.g., value maps, keypoints, or constraints) to ground language into executable motions. Hamster [29] fine-tunes a high-level VLM to produce a coarse 2D path that guides a low-level, 3D-aware control policy. VoxPoser [11] leverages the code-writing capabilities of Large Language Models (LLMs) to compose 3D value maps grounded in the observation space, enabling model-based planning of closed-loop trajectories. MOKA [30] uses mark-based visual prompting to represent affordances as point sets, converting keypoint prediction into VLM-friendly queries. CoPa [31] decomposes manipulation into task-oriented grasping and task-aware motion planning by extracting part-level geometric constraints for post-grasp poses. ReKep [10] represents tasks as relational keypoint constraints expressed as functions and solves them via hierarchical optimization. Finally, OmniManip [32] proposes a zero-training approach based on object-centric canonical spaces and functional affordances.

While promising, these approaches face practical challenges in open-world deployment. Many rely on multi-view sensing or careful scene setups that are difficult to maintain, especially for mobile manipulators. In addition, keypoint- and constraint-based formulations often require embodiment-specific optimization and tuning, which can hinder cross-embodiment transfer and long-horizon robustness. Finally, failure recovery is often limited because verification and causal analysis are not deeply integrated into the planning-execution loop.

C. Manipulation Failure Detection and Autonomous Recovery

Robustness to execution failures is essential for long-horizon robotic manipulation [33], [34], particularly under

zero-shot conditions. Existing work on failure detection and recovery can be broadly categorized into data-driven and model-based approaches. Data-driven methods learn to detect or recover from failures using sensory feedback, e.g., via reinforcement learning for adaptive behaviors or supervised classification of failure modes. A modular hierarchical framework is proposed by decoupling manipulation into base task-oriented skills and reinforcement learning (RL)-based failure prevention skills [35]. Moreover, RecoveryChaining [36] employs hierarchical RL to learn recovery policies that, when triggered by failure detection, return the robot to a state where nominal model-based controllers can resume the task. In a supervised setting, FINO-Net [37] utilizes multimodal sensor fusion to detect anomalies, though it relies on datasets restricted to a limited set of manually classified and rigid error types. In contrast, model-based methods rely on explicit heuristic functions [12] or sensors of the robot [38] to detect discrepancies between expected and observed outcomes, often by monitoring execution constraints or key performance indicators and triggering corrective actions when violations occur. Both paradigms have limitations: learning-based methods can struggle to generalize to unseen failure modes, while model-based pipelines may be computationally expensive and may not capture complex contact dynamics. These limitations motivate our reflective recovery mechanism, which leverages VLM-based semantic verification [39] together with structured memory to support diagnosis and replanning during long-horizon or complicated execution.

III. EMBODIED AGENTIC STRUCTURE FOR ROBOTIC MANIPULATION

In this section, we formulate the problem of robotic manipulation and detail the architecture of our proposed embodied AI agent. We focus on the semantic parsing of unstructured environments and the coordination mechanism that bridges high-level reasoning with low-level control.

A. Problem Statement

We formulate robotic manipulation as a sequential decision-making problem over a horizon T , where an agent selects actions $a_t \in \mathcal{A}$ at discrete time steps $t \in \{0, 1, \dots, T-1\}$ to drive the environment from an initial state $s_0 \in \mathcal{S}$ toward a goal specification s_g (or, more generally, a goal set $\mathcal{S}_g \subseteq \mathcal{S}$). The resulting trajectory is denoted by the sequence $\tau = (s_0, a_0, s_1, a_1, \dots, s_T)$, where state transitions are governed by the stochastic transition dynamics $P(s_{t+1} | s_t, a_t)$ of the underlying Markov Decision Process (MDP). The objective is to find a policy $\pi : \mathcal{S} \times \mathcal{S}_g \rightarrow \mathcal{A}$ that maximizes the probability of successfully and safely completing the task.

Specifically, long-horizon tasks exhibit strong *sequential dependency*: failures or small deviations at early steps can invalidate later actions. If we define an atomic-step success event E_t , e.g., satisfying a pre-/post-condition for a_t , the episode success probability can be expressed as

$$P(\text{success}) = P\left(\bigcap_{t=0}^{T-1} E_t\right) = \prod_{t=0}^{T-1} P(E_t | E_{0:t-1}), \quad (1)$$

which typically decreases as the horizon grows. This motivates explicit verification and recovery mechanisms to mitigate error accumulation during execution.

The system utilizes a constrained perception suite and free-form textual commands to facilitate universal deployability across diverse, unstructured environments. The robot perceives the workspace using a single wrist-mounted RGB-D camera, producing an ego-centric observation $\mathcal{I}_w \in \mathbb{R}^{H \times W \times 4}$. We deliberately exclude static third-person views to avoid external instrumentation and to support mobile deployment. Furthermore, the task is specified by a free-form natural language command \mathcal{L}_h , which must be semantically grounded into executable operations. The control output is defined in the end-effector (EEF) Cartesian space: an action a_t specifies a target EEF pose, represented as $\mathbf{p}_t = [x, y, z, q_w, q_x, q_y, q_z]^\top \in \mathbb{R}^7$, where $[x, y, z]$ denotes position and $[q_w, q_x, q_y, q_z]$ denotes a unit quaternion for orientation.

B. Agentic AI Coordinated Workflow

To address the complexity of long-horizon tasks, we propose a hierarchical agentic workflow that decouples semantic reasoning from geometric execution. We first define the structured world model used for grounding and then describe how the agent plans and executes long-horizon behaviors on top of it.

1) *Semantic-Operational State Graph (SOSG)*: The SOSG serves as the structured world model for our manipulation framework, as illustrated in the bottom panel of Fig. 3. We denote the graph as $\mathcal{G} = (\mathcal{V}, \mathcal{E})$. The node set $\mathcal{V} = \{v_i\}_{i=1}^n$ represents physical entities in the workspace. Each node v_i is parameterized by an augmented state vector $\mathbf{x}_i \in \mathcal{X}$ that encapsulates geometric, kinematic, and semantic properties needed for motion synthesis:

$$\mathbf{x}_i = [\mathcal{S}_i, \mathcal{K}_i, \mathcal{A}_i, \mathcal{P}_i]^\top. \quad (2)$$

The components are defined as follows:

- $\mathcal{S}_i = \{l_i, r_i, \tau_i\}$ represents the **semantic configuration**, comprising the object class l_i , its operational role r_i (e.g., container, manipulatable object), and a natural language context τ_i for high-level task planning.
- $\mathcal{K}_i = \{\alpha_i, w_i, \mathcal{R}_i\}$ defines the **kinematic and spatial constraints**, where $\alpha_i \in \{0, 1\}$ indicates whether the object is articulated (i.e., possessing internal degrees of freedom such as prismatic joints), $w_i \in \mathbb{R}^+$ specifies a characteristic grasping aperture for stable prehension, and \mathcal{R}_i denotes the pose relative to the robot base frame \mathcal{F}_b .
- $\mathcal{A}_i = \{c_i, \zeta_i, m_i\}$ captures **intrinsic physical attributes**, including color c_i , geometry/shape ζ_i , and material properties m_i , which inform contact and interaction strategies.
- $\mathcal{P}_i = \{(p_k, \delta_k)\}_{k=1}^K$ defines the **operational part decomposition**, mapping sub-components p_k to functional descriptions δ_k for part-centric manipulation (e.g., grasping a drawer handle).

By embedding these physical and semantic priors into \mathbf{x}_i , the SOSG provides a unified representation that bridges high-level symbolic planning with low-level position control. The edges $\in \mathcal{E}$ are dynamically adapted, constructed by tool invocation.

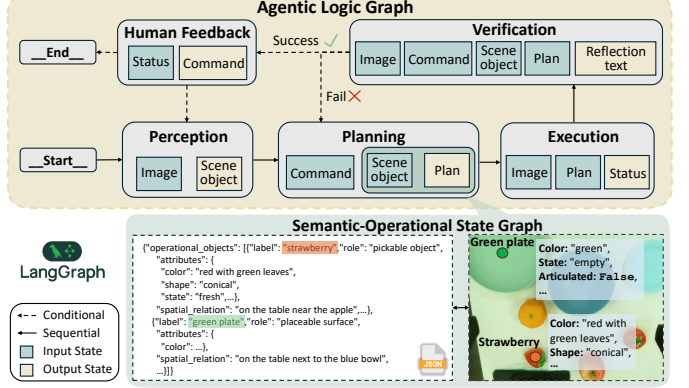


Fig. 3: The structure and workflow of the proposed bi-level agentic operational graph. The upper layer shows the AI agent with five nodes and conditional directed edges as the ALG. The lower layer shows the structured semantic understanding of the environment described by the SOSG.

2) *Agentic Task and Action Planning*: Building on the SOSG, the Agent Logic Graph (ALG) follows a *Perceive-Plan-Act-Reflect* cycle, as illustrated in the top panel of Fig. 3. Given a natural language command \mathcal{L}_h and the available tool library \mathcal{T}_c , the agent first perceives the scene and instantiates/updates \mathcal{G} . It then decomposes the long-horizon objective into a sequence of executable sub-tasks and executes each sub-task by invoking modules for spatial reasoning, affordance generation, and collision-free motion planning. The toolset \mathcal{T}_c is conditioned on the robot configuration $c \in \{\text{fixed, mobile}\}$. Specifically, we define $|\mathcal{T}_{\text{fixed}}| = 2$ and $|\mathcal{T}_{\text{mobile}}| = 3$, reflecting the varying operational capabilities of each platform, detailed in Section IV-B. Crucially, the workflow maintains a reflection loop: if a sub-task fails, the agent retrieves recent interaction history as the episodic memory to diagnose the cause and replan, rather than halting.

3) *Agentic Spatial Reasoning and Action Parameterization*: To translate high-level intent into physical execution, the agent performs fine-grained spatial reasoning by grounding the command \mathcal{L}_h into specific nodes within the SOSG. This process identifies task-relevant objects to compute the affordance \mathcal{A}_{ff} and its corresponding 7-DoF grasp/release offset $\mathcal{J} = \{\mathbf{t}, \mathbf{R}, w\}$, where $\mathbf{t} \in \mathbb{R}^3$ and $\mathbf{R} \in SO(3)$ represent the translation and orientation, and w denotes the target gripper aperture. This parameterization bridges the gap between semantic intent and the geometric constraints of the workspace. Once \mathcal{J} is determined, the agent coordinates the motion planning function f_{plan} to generate an executable trajectory:

$$\mathcal{W} = f_{\text{plan}}(\mathbf{p}_s, \mathbf{p}_t, \mathcal{M}_{\text{occ}}) \quad (3)$$

where \mathbf{p}_s and \mathbf{p}_t are the starting and target EEF poses, and \mathcal{M}_{occ} is the occupancy representation derived from RGB-D inputs. The output $\mathcal{W} = \{\mathbf{w}_1, \mathbf{w}_2, \dots, \mathbf{w}_k\}, \mathbf{w}_i \in \mathbb{R}^7$, is a sequence of collision-free waypoints that ensures safe navigation through the environment. By delegating trajectory generation to this module, the agent abstracts low-level obstacle avoidance from its high-level reasoning flow. Specific implementation details regarding the planner and inverse kinematics are provided in Section IV.

IV. INTEGRATED AGENTIC GRAPH EXECUTION FOR ROBOTIC MANIPULATION

This section details how UniManip realizes a complete agentic operational graph. By leveraging the ALG as procedural memory and the SOSG as grounded episodic memory, the framework systematically achieves grounded scene parsing, action abstraction, safety-aware motion synthesis, and closed-loop reflection. It ensures that the robot remains synchronized with the physical environment even as tasks increase in complexity.

A. Graph-Grounded Scene Parsing and Task Decomposition

1) *Task Decomposition*: The task planning module bridges the free-form command \mathcal{L}_h with the agent's episodic world model $\mathcal{G} = (\mathcal{V}, \mathcal{E})$. Concretely, the ALG maps \mathcal{L}_h and the available tool library \mathcal{T}_c into a sequence of graph-conditioned sub-tasks, each represented as an operation over nodes (and parts) in $\mathcal{V} \cup (\bigcup_{i=1}^n \mathcal{P}_i)$.

A sub-task is encoded as either a directed edge e_{ij} or a self-loop e_{ii} with associated continuous parameters: **Transit operations**, illustrated as the first tool in the bottom left panel of Fig. 2, are represented by directed edges e_{ij} and correspond to a *move_to* operation, $\mathbf{M}(v_i, \mathbf{g})$, which moves the end-effector from the state associated with v_i to a target configuration \mathbf{g} grounded on v_j . **Manipulation operations**, shown as the second tool in Fig. 2, are represented by self-loops e_{ii} and correspond to *operate* actuation, $\mathbf{O}(\mathbf{t}, \mathbf{r})$, where

$$\begin{cases} \mathbf{t} = [\delta_x, \delta_y, \delta_z]^\top, & \text{w.r.t. } \mathcal{F}_i \\ \mathbf{r} = [\delta_{roll}, \delta_{pitch}, \delta_{yaw}]^\top, & \text{w.r.t. } \mathcal{F}_k \end{cases} \quad (4)$$

denote rotation and translation values. Note that $\mathcal{F}_i, \mathcal{F}_j \in \{\mathcal{F}_b, \mathcal{F}_e\}$, where \mathcal{F}_e is the EEF frame. This operation drives the EEF to execute relative motions along specified axes of the assigned Cartesian frame. For instance, for the task of opening a drawer, the corresponding motion representations are illustrated in Fig. 4. This graph-based motion representation makes the plan explicit, compositional, and amenable to verification and re-structuring during reflection.

2) *Dynamic SOSG Update and Scene Parsing*: To maintain consistency between the internal episodic world model and the physical environment, the SOSG is updated online during execution. The primary attribute requiring real-time refinement is the object pose \mathcal{R}_i (and, when applicable, part states in \mathcal{P}_i). We adopt a hierarchical open-vocabulary perception pipeline to update these attributes: **Coarse retrieval**: given the natural language context τ_i in \mathcal{S}_i and the current observation \mathcal{I}_w , an open-vocabulary detector proposes candidate regions $\{\mathbf{B}_k\}$ aligned with τ_i [40]. Candidates exceeding a confidence threshold τ_d are retained as region proposals \mathbf{B}^* . **Fine refinement**: a promptable segmentation model refines \mathbf{B}^* into a pixel-accurate mask \mathcal{M}_{seg} [41]. Together with the synchronized depth channel in \mathcal{I}_w , this mask enables robust 3D pose estimation and grasp perception. Concurrently, this unified pipeline facilitates affordance detection, allowing the updated 3D pose \mathcal{R}_i of the target object to be seamlessly integrated into the SOSG. This approach ensures robust state tracking even in the presence of clutter and partial occlusion.

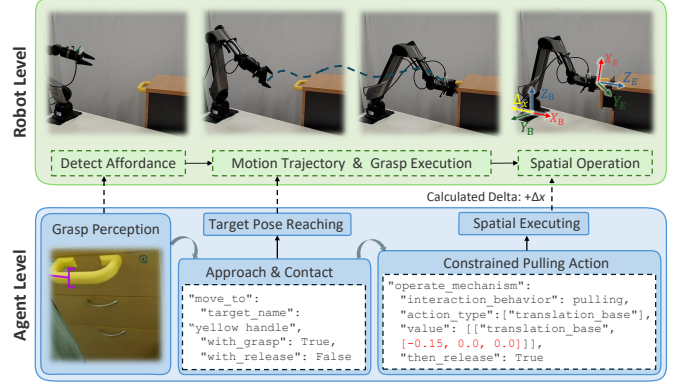


Fig. 4: Demonstration of the spatial operations of the robot, with an instance of opening a drawer. The task is decomposed into several tool invocations, and each tool has its specific spatial operational formats for the movement of the robotic manipulator.

For articulated objects ($\alpha_i = 1$), the agent additionally maintains an episodic mechanism state over operational parts $\{\delta_k\}_{k=1}^K$ in \mathcal{P}_i (e.g., *upper drawer: open*). This state is refreshed after each interaction and provides the agentic logic layer with grounded, temporally consistent pre-/post-conditions for subsequent planning.

B. Action Abstraction through Agentic Operational Primitives

The agentic graph executes the planned sub-tasks by invoking tools from the primitive library \mathcal{T}_c that implements atomic spatial operations under clear geometric semantics [42]. Each tool takes structured inputs grounded on the current SOSG \mathcal{G}_τ and returns parameters that can be tracked by the low-level controller. In the fixed-base setting,

$$\mathcal{T}_c = \{\mathbf{M}(v_i, \mathbf{g}), \mathbf{O}(\mathbf{t}, \mathbf{r}), \dots\} \quad (5)$$

primarily consists of *objective-oriented* motion and *operation-oriented* motion, as referred in Section IV-A1. This separation allows the agentic logic layer to compose long-horizon behavior as sequences of *goal-directed* and *constraint-directed* spatial operations while keeping the execution consistent.

Without loss of generality, the same abstraction extends to other robot morphologies by adding embodiment-specific tools without changing the task-level representation. Specifically, a mobile manipulator need an augmented library \mathcal{T}_{mobile} with a navigation primitive

$$\mathbf{N}(\mathcal{O}_{target}, \hat{d}_{obj}, d_{goal}) \in \mathcal{T}_{mobile}, \quad (6)$$

where \mathcal{O}_{target} denotes the target entity to dock to, \hat{d}_{obj} is the estimated real-time distance from the base to the target (obtained online from the ego-centric observation), and d_{goal} is the desired docking clearance. This primitive drives the base to a manipulation-feasible configuration, after which the same manipulation tools in \mathcal{T}_c can be invoked with unchanged semantics. The specific tools are detailed as follows.

1) *Objective-Oriented Motion*: This tool directs the EEF to a spatial target grounded on the current SOSG \mathcal{G}_τ . Its inputs include a target pose $\mathcal{R}_{target} \in SE(3)$ associated with a node $v_i \in \mathcal{V}$, together with boolean flags $b_{grasp}, b_{release} \in \{0, 1\}$

indicating whether a gripper action should be triggered upon arrival. The tool invokes the collision-free motion planner (Section IV-C) to generate a feasible trajectory, and outputs a trackable trajectory segment \mathcal{T}_{seg} executed by the low-level advanced controller.

2) *Operation-Oriented Motion*: This tool executes precise relative motions specified by metric constraints, which is essential for interaction-centric tasks such as pushing, pulling, twisting, or wiping. The input consists of a reference frame $\in \{\mathcal{F}_b, \mathcal{F}_e\}$ (base frame or end-effector frame) and a 6-DoF motion increment denoted in (4), which encodes translation and rotation along the axes of specific frames. Let $T_{curr} \in SE(3)$ denote the current EEF pose. We construct an incremental transform $\Delta T(\delta) \in SE(3)$ based on the operation values in (4) and compute the target pose by left- or right-multiplication depending on the chosen reference frame:

$$\begin{cases} T_{new} = \Delta T(\mathbf{t}, \mathbf{r}) T_{curr}, & \text{w.r.t. } \mathcal{F}_b \\ T_{new} = T_{curr} \Delta T(\mathbf{t}, \mathbf{r}), & \text{w.r.t. } \mathcal{F}_e \end{cases} \quad (7)$$

This formulation provides a uniform interface for part-centric operations (e.g., pulling a drawer along an axis) while remaining compatible with downstream trajectory generation and closed-loop verification.

C. Agenetic-Guided Motion Synthesis

Following the operational primitives, the safety-aware motion generation maps a target EEF pose to a collision-free waypoint sequence in Cartesian coordinate \mathcal{F}_b . Our design targets *single-view* deployment and therefore explicitly accounts for occlusion-induced uncertainty by constructing a conservative free space.

1) *Defensive Reconstruction of Occluded Areas*: Given a single RGB-D observation \mathcal{I}_w , we first reconstruct a conservative volumetric occupancy map that mitigates the *floating obstacle* issue caused by self-occlusions (e.g., unobserved cavities behind object rims). Let \mathcal{P}_{raw} denote the raw point cloud back-projected from \mathcal{I}_w . We discretize the workspace into a voxel grid with resolution r (meters) and define an occupancy map

$$\mathcal{M}_{init} : \{0, \dots, H-1\} \times \{0, \dots, W-1\} \times \{0, \dots, D-1\} \rightarrow \{0, 1\}, \quad (8)$$

where a voxel indexed by $\mathbf{u} = [u, v, w]^\top$ is marked occupied if any point in \mathcal{P}_{raw} falls within its spatial cell. In all experiments we use $r = 0.01$ m to balance accuracy and efficiency.

To reduce sensor noise and fill small holes on observed surfaces, we apply 3D morphological closing with a structuring element (kernel) \mathcal{K} ,

$$\mathcal{M}_{closed} = \mathcal{M}_{init} \bullet \mathcal{K} = (\mathcal{M}_{init} \oplus \mathcal{K}) \ominus \mathcal{K}, \quad (9)$$

where \oplus and \ominus denote dilation and erosion, respectively. For manipulation in tabletop and indoor scenes, we adopt a conservative safety heuristic that enforces vertical support under occupied voxels. Specifically, if a voxel is occupied, all voxels below it along the gravity axis are treated as non-traversable. The core objective is to constrain the planner from

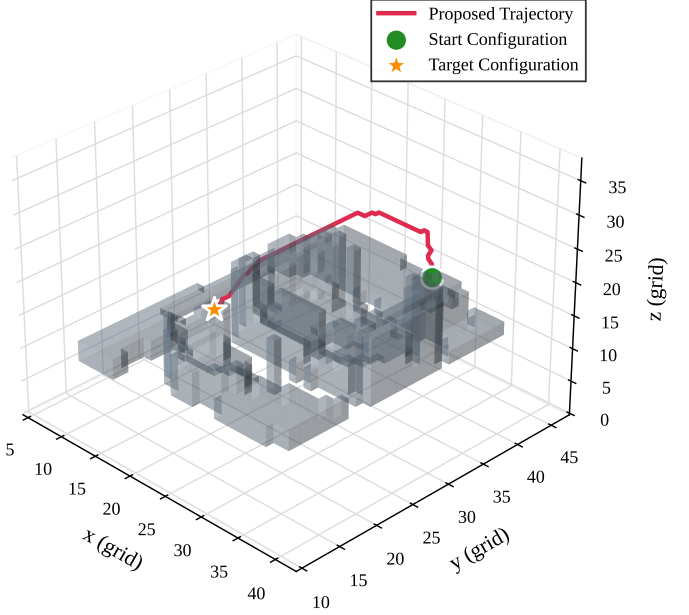


Fig. 5: Visualization of the conservative volumetric occupancy grid \mathcal{M}_{final} generated from a single-view RGB-D observation. The gravity-aligned completion over-approximates unknown space, improving safety under occlusion.

traversing unobserved cavities where occupancy is probable, such as the occluded space beneath a basket's rim, thereby mitigating collision risks in partially mapped environments. The final conservative map is

$$\mathcal{M}_{final}(u, v, w) = \bigvee_{k=w}^{D-1} \mathcal{M}_{closed}(u, v, k), \quad (10)$$

where \bigvee is the logical *or*. Fig. 5 visualizes an optimized trajectory example along with the reconstructed occupancy grid in the scenario with an obstacle blocking the EEF from the object to the target container, shown in Fig. 6(a).

2) *Safety-Aware Trajectory Generation*: We convert the conservative occupancy \mathcal{M}_{final} into an Euclidean signed distance field (ESDF) Φ , where each grid location is assigned its distance to the nearest occupied voxel:

$$\Phi(\mathbf{u}) = \text{dist}(\mathbf{u}, \{\mathbf{u}' \mid \mathcal{M}_{final}(\mathbf{u}') = 1\}). \quad (11)$$

This representation induces a smooth clearance metric that can be queried efficiently during planning. Let \mathbf{u}_s and \mathbf{u}_g denote the start and goal grid indices corresponding to the start and target EEF poses. We compute a discrete path $\mathcal{P}^* = [\mathbf{u}_0, \dots, \mathbf{u}_L]$ using A* algorithm [43] with objective:

$$f(\mathbf{u}) = g(\mathbf{u}) + h(\mathbf{u}), \quad (12)$$

where g is the accumulated edge cost and h is an admissible heuristic to \mathbf{u}_g . Specifically, Fig. 6(b) illustrates a sliced ESDF heat map derived from the conservative occupancy grid, highlighting clearance values from obstacles in the environment. Note that we enforce collision avoidance by requiring a clearance $r_{safe} > 0.05$ m at each expanded node,

$$V(\mathbf{u}) = \mathbb{I}[\Phi(\mathbf{u}) \geq r_{safe}], \quad (13)$$

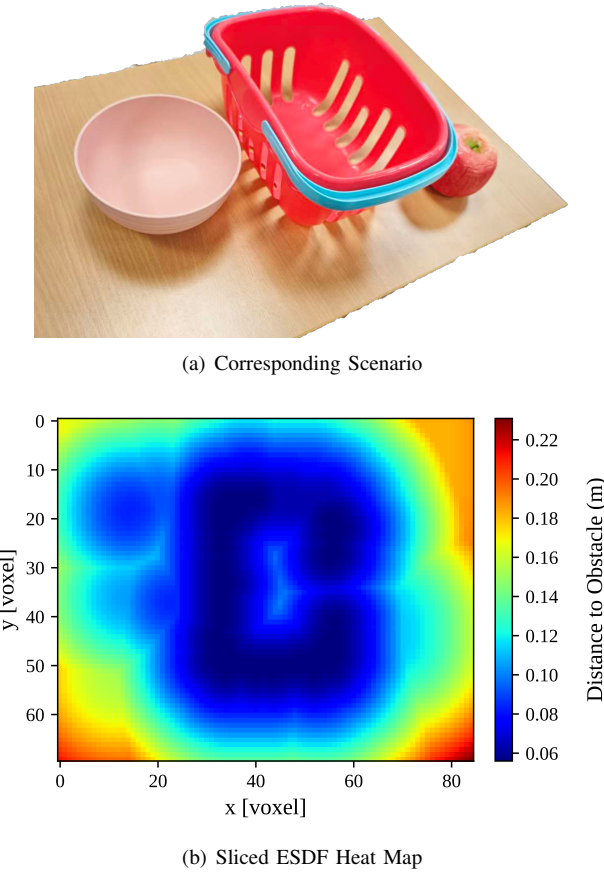


Fig. 6: The corresponding scene and a sliced ESDF illustrating clearance values from obstacles.

where $\mathbb{I}[\cdot]$ is the indicator function. This EEF trajectory generation approach is equivalent to planning in a free space eroded by a ball of radius r_{safe} (i.e., a conservative configuration-space dilation) without explicitly constructing the Minkowski sum.

The discrete path \mathcal{P}^* is mapped to metric coordinates in the base frame \mathcal{F}_b as $\mathbf{p}_i = r \cdot \mathbf{u}_i + \mathbf{p}_{\text{origin}}$, for $i = 0, \dots, L$, where $\mathbf{p}_{\text{origin}}$ denotes the world coordinates of the voxel grid origin. To extend the discrete geometric path $\{\mathbf{p}_i\}$, initially defined only by Cartesian positions, into a full 6-DOF end-effector trajectory, we perform orientation synthesis via Spherical Linear Interpolation (Slerp) [44]. Let $\xi_s, \xi_g \in S^3$ denote the unit quaternions representing the initial and goal orientations, respectively. For each waypoint \mathbf{u}_i , we define the interpolation parameter $\alpha = i/L$. The synthesized orientation ξ_i is computed to traverse the shortest geodesic arc on the unit hypersphere:

$$\text{Slerp}(\xi_s, \xi_g; \alpha) = \frac{\sin((1-\alpha)\theta)}{\sin \theta} \xi_s + \frac{\sin(\alpha\theta)}{\sin \theta} \xi_g, \quad (14)$$

where $\theta = \arccos(\xi_s \cdot \xi_g)$ is the angle between the orientations. To ensure the shortest path is taken on S^3 , we enforce the condition $\xi_s \cdot \xi_g \geq 0$, negating ξ_g if necessary to account for the double-cover property of $SO(3)$. This synthesis produces a trajectory that exhibits smooth rotational transitions while preserving the safety clearance established by the ESDF.

3) Relaxed Inverse Kinematics for Waypoint Tracking:

While the collision-free motion planner outputs a geometric waypoint sequence $\mathcal{W} = \{\mathbf{w}_1, \dots, \mathbf{w}_k\}$ in task space, executing this path requires solving inverse kinematics to map each desired end-effector pose to a joint configuration $\mathbf{q} \in \mathbb{R}^n$. In practice, standard IK solvers can fail when a waypoint is close to a kinematic singularity, lies marginally outside the reachable workspace, or requires an orientation that is difficult to realize under joint limits. Because the waypoint generator is agnostic to the arm's kinematic feasibility set, such failures can halt long-horizon execution even when a nearby pose would be sufficient for safe progress.

To address this issue, we adopt a *parameter-relaxed* IK strategy that prioritizes continuity of execution over exact pose matching in kinematically challenging regions. Let $\mathbf{p}(\mathbf{q}) \in \mathbb{R}^3$ and $\xi(\mathbf{q}) \in S^3$ denote the forward kinematics position and unit quaternion orientation of the end-effector, respectively, where $\mathbf{q} \in \mathbb{R}^n$ is the joint angle vector. Given a desired pose, the optimal joint configuration \mathbf{q}^* is obtained by solving:

$$\mathbf{q}^* = \arg \min_{\mathbf{q}} \lambda_p \|\mathbf{p}(\mathbf{q}) - \mathbf{p}_{\text{des}}\|_2^2 + \lambda_r \|\xi(\mathbf{q}) \ominus \xi_{\text{des}}\|_2^2 \quad (15)$$

subject to joint-limit constraints:

$$\mathbf{q}_{\min} \preceq \mathbf{q} \preceq \mathbf{q}_{\max}, \quad (16)$$

and nominal convergence tolerances:

$$\|\mathbf{p}(\mathbf{q}) - \mathbf{p}_{\text{des}}\|_2 < \epsilon_p, \quad \|\xi(\mathbf{q}) \ominus \xi_{\text{des}}\|_2 < \epsilon_r. \quad (17)$$

Here, $\lambda_p, \lambda_r > 0$ are weighting coefficients, and \ominus denotes a geodesic orientation-error operator on $SO(3)$, typically implemented via the quaternion logarithm or angle-axis distance. Many conventional IK implementations keep (ϵ_p, ϵ_r) fixed and tight (e.g., millimeter-level position tolerance), which can yield “no-solution” outcomes for waypoints that are only marginally infeasible due to voxelization or ESDF gradients.

We mitigate non-convexity via multi-seed initialization near the initial state and relax the tolerances only when necessary. The solver first attempts convergence under strict tolerances $(\epsilon_p^{(0)}, \epsilon_r^{(0)}) = (0.01 \text{ m}, 0.02 \text{ rad})$. If it fails to converge, we relax the tolerances according to

$$\epsilon_p^{(k+1)} \leftarrow 5 \epsilon_p^{(k)}, \quad \epsilon_r^{(k+1)} \leftarrow 2 \epsilon_r^{(k)}. \quad (18)$$

The loop terminates once a feasible solution is found or once (ϵ_p, ϵ_r) exceeds a predefined safety budget. To ensure a well-defined orientation error, we enforce quaternion normalization on the target, $\|\mathbf{q}_{\text{des}}\|_2 = 1$, before optimization. Overall, RIK yields a best-effort joint solution that preserves smooth execution and avoids dead-ends when the ideal waypoint is near the boundary of kinematic feasibility. This is particularly beneficial for different embodiments with varying kinematic structures and reachability profiles.

D. Agentic Verification and Autonomous Recovery

A core limitation of open-loop task execution is its fragility under partial observability and unmodeled contact dynamics: a single failed atomic operation can invalidate subsequent preconditions and cascade into long-horizon failure. UniManip

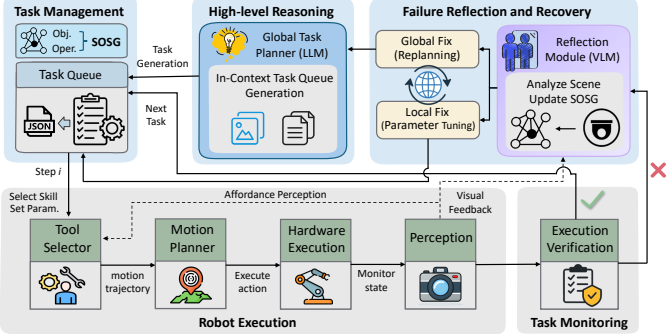


Fig. 7: The closed-loop failure reflection and recovery mechanism in UniManip. The system continuously monitors execution states, detects anomalies, and invokes high-level cognitive reasoning to diagnose and recover from failures, either through local corrections or global replanning.

addresses this by embedding execution into a closed-loop failure reflection and recovery mechanism. It couples procedural memory (deciding what to do, when to verify, and how to replan) in the *Tool Selector* of the agentic logic layer with the episodic memory (grounding the agent in object-centric, time-indexed world state) that functions in the Task Manager with SOSG \mathcal{G} . In this view, a failure is not a terminal outcome but a transitional state that triggers verification, diagnosis, and recovery actions conditioned on both the current observation and the structured execution trace stored in the AOG.

1) *Anomaly Detection and State Verification*: We represent a manipulation task \mathcal{T} (parsed from the free-form instruction \mathcal{L}_h) as an ordered sequence of atomic spatial operations

$$\mathcal{P}_{\text{ops}} = (o_1, o_2, \dots, o_N). \quad (19)$$

Let s_t denote the robot-environment execution state at time step t (including proprioception and the current episodic memory \mathcal{G}_t), and let \mathcal{I}_t denote the corresponding wrist RGB-D observation. We introduce a verification operator $\mathcal{F}_{\text{verify}}(s_t, \mathcal{I}_t, o_k)$ that evaluates whether the intended post-conditions of the current operation o_k are satisfied.

Concretely, verification combines two complementary modalities. *Geometric consistency* checks whether the measured robot state (e.g., end-effector pose, gripper state) satisfies the metric constraints implied by o_k (e.g., waypoint reachability, relative motion bounds). *Visual-semantic consistency* uses a VLM-based verifier to assess the post-execution observation and determine whether the SOSG (episodic memory) has transitioned as expected (e.g., an object is grasped, moved, or a drawer changes state).

The binary execution outcome is then defined as

$$E_t = \begin{cases} 1, & \text{if } \mathcal{F}_{\text{verify}}(s_t, \mathcal{I}_t, o_k) = \text{success}, \\ 0, & \text{otherwise.} \end{cases} \quad (20)$$

If $E_t = 0$, the agent transitions from open-loop execution to the reflective recovery loop.

2) *Agentic Reflection via Graph and Memory*: Upon a detected failure ($E_t = 0$), the agent initiates a reflection cycle that explicitly leverages the AOG as structured procedural memory. Let \mathcal{H}_t denote a short-term execution trace (e.g., the most recent operation nodes, tool inputs/outputs, and

verification results), and let \mathcal{M}_{ret} denote retrieved experience from long-term memory via retrieval-augmented generation. We model reflection as a transformation operator

$$(\mathcal{G}_t^{\text{ref}}, D_{\text{err}}) = \Psi(\mathcal{I}_t, \mathcal{H}_t, \mathcal{M}_{\text{ret}} \mid \text{Agent}), \quad (21)$$

where Ψ performs two coupled updates. First, it updates episodic memory by revising the SOSG state to $\mathcal{G}_t^{\text{ref}}$ (e.g., annotating a node/part state as “not grasped” or “drawer partially open”), ensuring that subsequent reasoning is grounded in the observed outcome rather than the intended one. Second, it produces a semantic diagnosis D_{err} (e.g., grasp slippage, collision, occlusion-induced mislocalization) that conditions the choice of recovery action in the agentic logic layer.

3) *Error-Informed Reflection and Agentic Recovery*: Conditioned on the diagnosis D_{err} and the reflected episodic state $\mathcal{G}_t^{\text{ref}}$, the ALG selects a recovery strategy at one of two levels. Crucially, the system leverages the residual error of the failed trajectory, derived from the discrepancy between the intended post-condition and the observed state, as a feedback signal to guide the subsequent repair.

For low-level deviations, such as minor pose errors, gripper slippage, or transient occlusions, the agent computes a corrective adjustment δo by back-projecting the execution error into the operation parameter space. The agent then reissues a repaired operation $o'_k = o_k \oplus \delta o$. This mechanism uses the failure offset as an informative prior to adjust action parameters (e.g., increasing gripper force or shifting a grasp pose), preserving the high-level task structure while repairing the physical realization.

On the contrary, for high-level divergences that invalidate future preconditions, such as target displacement or scene topology changes, the execution error acts as a state-update trigger. The system discards the remaining plan and regenerates a new operation sequence conditioned on the updated episodic memory, the free-form command \mathcal{L}_h , and retrieved experience \mathcal{M}_{ret} :

$$\mathcal{P}_{\text{new}} = \Pi(\mathcal{G}_t^{\text{ref}}, \mathcal{L}_h, \mathcal{M}_{\text{ret}}). \quad (22)$$

By embedding the failure context directly into $\mathcal{G}_t^{\text{ref}}$, the planner ensures that the new trajectory \mathcal{P}_{new} is physically consistent with the modified environment, preventing cyclic failures.

This recovery mechanism provides a structured procedural scaffold for the VLM to decide when to repair locally versus when to restructure the entire plan, ensuring long-horizon robustness through continuous feedback integration.

V. EXPERIMENTAL RESULTS AND ANALYSIS

A. Evaluation Goals and Environmental Setup

Our experiments evaluate UniManip along three axes: (1) zero-shot manipulation performance under unseen objects and distractors, (2) robustness in cluttered scenes compared with representative hierarchical open-vocabulary planners, and (3) long-horizon and interaction-rich tasks that stress verification and recovery. In addition, we report ablations that isolate the effects of collision-free planning, relaxed IK, and the reflection/recovery loop, and we demonstrate cross-embodiment transfer on a mobile manipulator without fine-tuning.

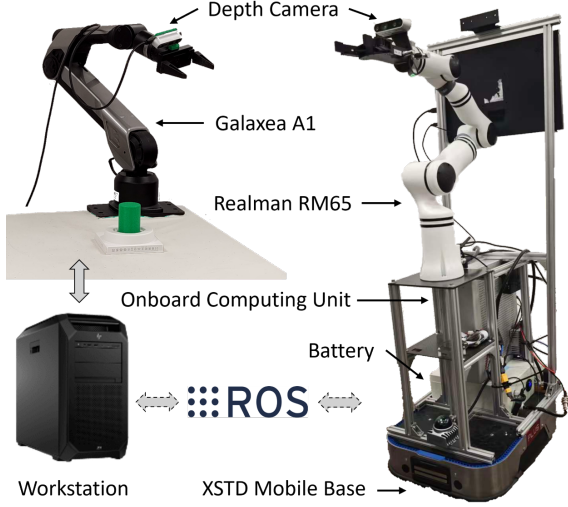


Fig. 8: The experimental setup featuring the Galaxeia A1 robotic arm with a two-finger gripper and RealSense D435 RGB-D camera mounted above the end-effector. A mobile manipulator equipped with Realman RM65 is also utilized for cross-embodiment evaluations.

The experiments are conducted using a Galaxeia A1 robotic arm (6-DoF) equipped with a two-finger gripper and an Intel RealSense D435 RGB-D camera mounted in an eye-in-hand configuration, as shown in Fig. 8. The workspace is arranged with diverse household objects to evaluate zero-shot generalization across object categories, spatial layouts, and task formats. All methods are executed on a workstation with an Intel i9-13900K CPU, an NVIDIA RTX 4080 GPU, and 32 GB RAM. The software stack uses ROS Noetic with PyTorch for learning-based components and NVIDIA cuRobo for GPU-accelerated optimization. For cross-embodiment evaluation, we additionally deploy UniManip on a mobile manipulator (right in Fig. 8) consisting of a differential-drive base and a Realman RM65 (6-DoF) arm. The same eye-in-hand RGB-D sensing setup is used, enabling evaluation under viewpoint changes induced by navigation.

B. Zero-shot Manipulation Performance

We compare our UniManip framework against three state-of-the-art VLA methods: π_0 [7], NORA [45], and NORA-1.5 [8]. These baselines represent the current leading end-to-end approaches in robotic manipulation using vision-language models. To facilitate fine-tuning of the baseline models, we curated a dataset comprising 1,000 demonstration episodes collected on a Galaxeia A1 robotic platform. While the baselines utilize a dual-camera configuration, consisting of a wrist-mounted Intel RealSense D435 and a third-person RealSense D515, our proposed method still operates using only the single wrist camera. Data were acquired via isomorphic teleoperation, covering nine distinct pick-and-place tasks with a distribution of approximately 110 episodes per task. To satisfy the input requirements of the VLA baselines, this experimental setup incorporates a third-view camera for global context and a wrist camera for localized manipulation cues. To ensure the robustness of the learned policies, we employed a

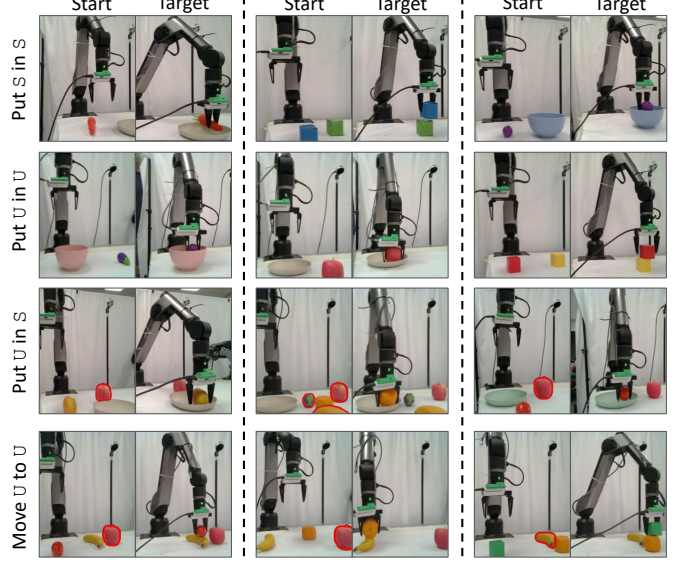


Fig. 9: The comparison scenarios with VLA models. The distractors (unseen objects during model training) are marked with red curves.

stochastic setup: objects were placed in unstructured configurations across the workspace without a predefined sequence, requiring the models to generalize across varied initial states and spatial relations. The evaluation (shown in Table I) focuses on a suite of manipulation tasks that vary in complexity and object familiarity. With the notation of U and S representing “Unseen” and “Seen” objects respectively, we categorize the tasks into four main types: “Put S in S ,” “Put U in U ,” “Put U in S ,” and “Move U to U .” As illustrated in Fig. 9, seen objects are those that were part of the training dataset, while unseen objects are novel items not encountered during training. To rigorously test the generalization capabilities of each method, we introduce distractor objects in the environment during the unseen tasks, as detailed in Table II. Each task category is designed to test the system’s ability to generalize to new objects and scenarios. The performance metrics used for comparison include the partial success rate (PSR), the distractor grasping rate (Dist.), and the success rate (SR). These metrics provide a comprehensive assessment of each method’s effectiveness in executing the specified manipulation tasks.

The results show that UniManip consistently outperforms end-to-end VLA baselines, with an average success rate (SR) of 93.75% compared to 71.25% for NORA-1.5-FAST (the strongest baseline). This gap is most pronounced in the U -involving categories (U in S and U to U), where the policy must generalize beyond the demonstrated object set.

These gains are enabled by two architectural choices.

Grounded task representation reduces distractor errors. UniManip achieves a much lower distractor grasping rate of 7.78%. This follows from the Bi-level AOG: the agentic logic layer queries the SOSG for object-centric constraints (identity, role, and spatial relations) before committing to a manipulation primitive. In contrast, end-to-end VLAs can overfit to co-occurrence patterns in demonstrations and may drift toward salient distractors when the distribution shifts.

TABLE I: Comparison with VLA Methods on Diverse Manipulation Tasks

Task Format	Task	π_0 [7]			NORA [45]			NORA-1.5 [8]			UniManip (Ours)		
		PSR↑	Dist.↓	SR↑	PSR↑	Dist.↓	SR↑	PSR↑	Dist.↓	SR↑	PSR↑	Dist.↓	SR↑
Put S in S	Put carrot in yellow plate	100	—	100	100	—	100	100	—	100	100	—	100
	put blue cube on green cube	90	—	80	90	—	90	100	—	90	100	—	90
	put eggplant in blue bowl	100	—	90	90	—	90	90	—	90	100	—	100
	Put mango in basket	90	—	90	90	—	90	90	—	90	100	—	90
Put U in U	Put eggplant in pink bowl	90	—	80	90	—	90	100	—	100	100	—	100
	Put apple in yellow plate	70	—	30	100	—	80	100	—	90	90	—	90
	Put red cube on yellow cube	70	—	70	90	—	70	90	—	80	90	—	80
Put U in S	Put strawberry in green plate	0	90	0	70	0	70	70	10	70	90	10	90
	Put grape in green plate	0	90	0	70	20	50	80	20	70	90	10	90
	Put orange in green plate	0	100	0	30	20	40	70	30	60	100	0	100
	Put mango in yellow plate	60	20	50	70	10	60	70	10	60	80	0	80
	Put orange in yellow plate	50	30	40	70	20	50	60	10	50	100	10	100
	Put orange in yellow plate	20	30	10	60	30	40	70	20	50	100	20	100
Move U to U	Move strawberry to banana	50	50	10	60	20	20	60	0	40	100	0	100
	Move orange to banana	50	30	10	80	0	50	70	20	50	90	20	90
	Move cube to orange	50	50	20	80	20	60	70	20	60	100	0	100
Average		55.63	60.00	41.88	76.88	15.56	63.13	83.13	15.56	71.25	95.63	7.78	93.75

Note: PSR indicates partial success rate (%) with grasping the correct object; Dist. indicates the rate (%) of grasping distractor objects; SR indicates overall task success rate (%).

TABLE II: Detailed Distractor Configurations for Unseen Object Manipulation Scenarios

Task Format	Objects of Interest		Distractor(s)
	Target	Container	
Put U in S	strawberry	green plate	apple
	grape	green plate	eggplant
	orange	green plate	banana
	mango	yellow plate	apple
	orange	yellow plate	apple and grape
	orange	yellow plate	apple, grape and mango
Move U to U	strawberry	banana	apple
	orange	banana	apple
	cube	orange	banana

Explicit task-to-motion bridging improves execution reliability. Even when the target is correctly identified (high PSR), end-to-end policies can fail due to stuck to local optima or collisions during approach. UniManip parameterizes each operation through (a) conservative occupancy completion under single-view occlusion and (b) safety-aware planning, followed by relaxed IK tracking when strict IK is infeasible. This makes the final motion physically consistent with the scene, improving SR beyond purely semantic correctness.

C. Robustness Evaluation in Cluttered Scenarios

We further evaluate UniManip against representative hierarchical open-vocabulary manipulation frameworks, including ReKep [10], MOKA [30], and VoxPoser [11], as shown in Table III. The benchmark focuses on cluttered desktop scenes with multiple distractors (Table IV), which stress both semantic grounding (selecting the correct target/container) and geometric feasibility (collision-free reaching and placement under clutter). The evaluation results report the task success rate (TSR). UniManip achieves 82.5%, substantially higher than ReKep (47.5%), MOKA (57.5%), and VoxPoser (55.0%). We attribute the gain to two factors:

The AOG architecture enhances task resilience through plan adaptation. In clutter, a correct high-level plan is insufficient: intermediate outcomes must be verified, and the remaining plan must be updated when the world changes (e.g., an object is displaced during grasp). UniManip’s AOG explicitly stores operation-level context (tool inputs/outputs and expected post-conditions) and couples it with the objects’ states, allowing the system to detect deviations and either locally repair or globally replan. Baselines that rely on a single-pass plan (or weak verification) tend to cascade failures once an early step drifts.

Task-to-motion bridge reduces geometric brittleness. Current hierarchical methods produce goal representations (keypoints, value maps, or constraints) but can still be brittle when the generated motion is marginally infeasible or unsafe. UniManip explicitly accounts for occlusion-induced uncertainty through conservative occupancy completion and plans with safety-aware clearance constraints, then uses relaxed IK to avoid dead-ends near singularities. This reduces collisions and IK failures that otherwise dominate in clutter.

Finally, UniManip’s compact tool interface (as a demonstration in Fig. 4) reduces the burden on the foundation model: the VLM is primarily used for high-level decomposition and verification, while geometric feasibility is handled by dedicated planning modules. This makes the pipeline compatible with smaller VLMs (e.g., Qwen-3-VL-4B [46] utilized in this paper) and supports practical deployment with limited onboard compute.

D. Evaluation on Long-Horizon and Dexterous Tasks

While the previous comparisons mainly test short-horizon pick-and-place capability, we additionally evaluate UniManip on long-horizon and interaction-rich tasks that are typically out-of-scope for VLA and the hierarchical baselines. These scenarios require (1) sequential composition of heterogeneous skills, (2) precise contact control and geometric safety in

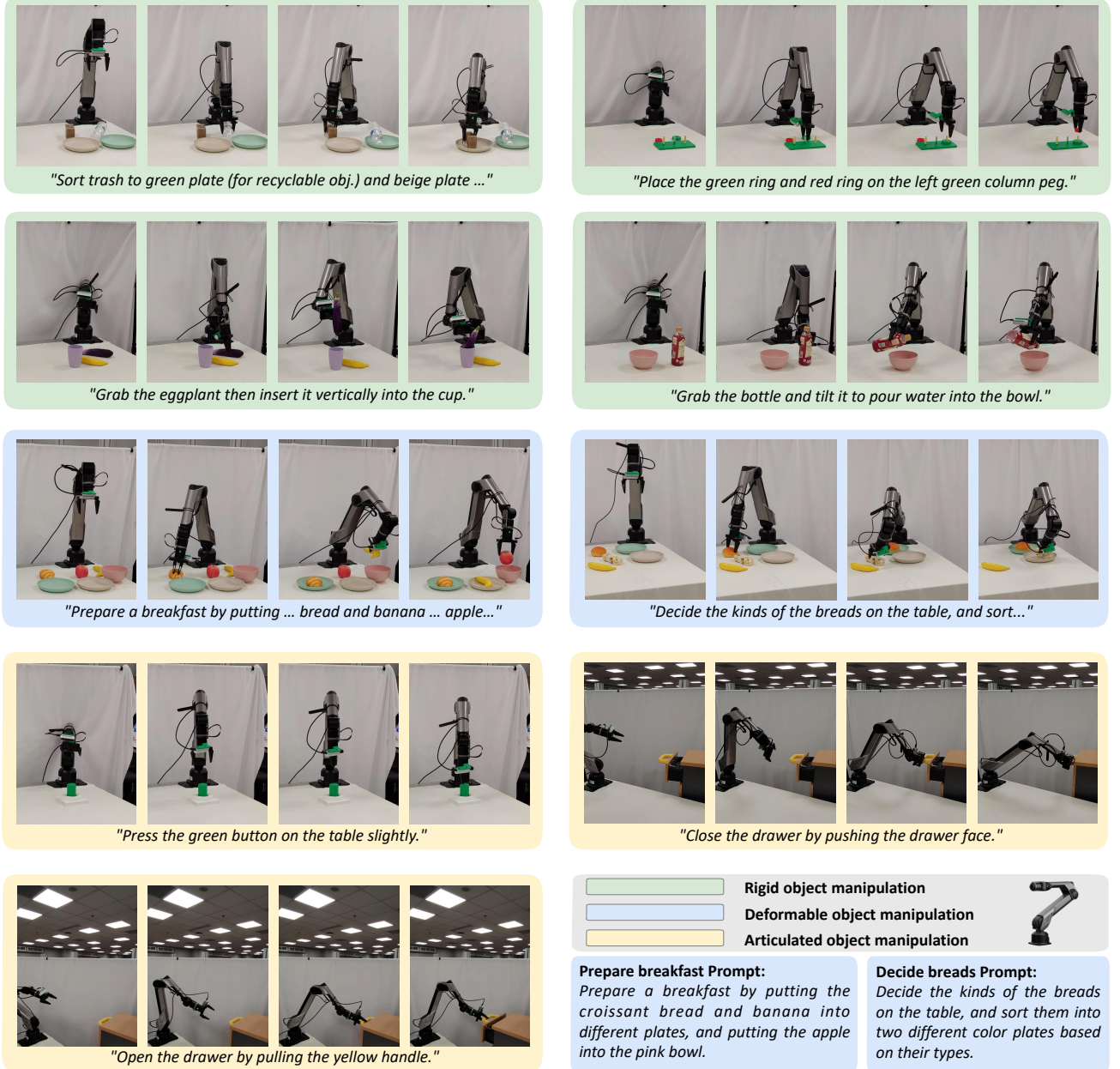


Fig. 10: Demonstration of UniManip executing various manipulation tasks in a cluttered desktop environment. The robot successfully performs tasks such as sorting trash, inserting objects, pouring water, preparing breakfast, and opening/closing drawers, showcasing its versatility and robustness.

TABLE III: Comparison with Hierarchical Methods on Benchmark Tasks in Cluttered Desktop Environment

Task	ReKep [10]	MOKA [30]	VoxPoser [11]	Ours
Put orange in blue bowl	60	60	50	80
Put apple in beige plate	60	60	70	90
Put tomato in basket	20	80	70	90
Put strawberry in basket	40	20	60	60
Put pepper in blue plate	40	60	40	70
Put carrot in green plate	80	60	60	90
Put banana in blue plate	40	60	40	90
Put cucumber in green plate	40	60	50	90
Average	47.50	57.50	55.00	82.50

clutter, and (3) closed-loop recovery when intermediate steps fail. The execution traces for these representative manipulation tasks are visualized in Fig. 10.

TABLE IV: Detailed Distractor Configurations for Cluttered Object Manipulation Scenarios

Target	Objects of Interest		Distractor(s)
	Target	Container	
orange	blue bowl	strawberry, apple, tomato, green plate, azure plate	
apple	beige plate	orange, strawberry, tomato, blue bowl, green plate	
tomato	basket	carambola, orange, blue plate, blue bowl	
strawberry	basket	carambola, orange, azure plate, blue plate, blue bowl	
pepper	blue plate	carrot, azure plate, blue bowl, green plate	
carrot	green plate	eggplant, azure plate, blue bowl, blue plate	
banana	blue plate	eggplant, azure plate, blue bowl, green plate	
cucumber	green plate	banana, blue plate	

To evaluate the versatility of UniManip, we conducted experiments across eight distinct scenarios categorized by their physical properties and interaction requirements. **Rigid**

TABLE V: **Ablation Settings.** We evaluate three configurations (V1, V2, V3) to analyze the contribution of each module. (✓: Included, ✗: Excluded)

Feature	V1	V2	V3
Parameter-relaxed Inverse Kinematics (RIK)	✓	✓	✓
Collision-Free Planning (CFP)	✗	✓	✓
Failure Detection & Recovery (FDR)	✗	✗	✓

object manipulation tasks focus on precision and geometry-aware placement, including the sorting of waste items (e.g., plastic bottles and batteries) into designated bins, the insertion of geometric shapes into poled bases, and the placement of elongated objects into narrow apertures. This category also evaluates controlled interactions, such as pouring water from a bottle into a bowl. We further assess **deformable object interaction** through the sorting of diverse bread types and a multi-stage breakfast preparation sequence requiring the handling of soft food items through coordinated pick-and-place and tool-use motions. Finally, **articulated-object interaction** is evaluated through button-pressing under tight positional tolerances and the execution of drawer opening and closing sequences involving robust state verification.

To isolate which components drive performance, we ablate three execution-critical modules: Parameter-relaxed Inverse Kinematics (RIK), Collision-Free Planning (CFP), and Failure Detection & Recovery (FDR). The specific configurations for these variants are detailed in Table V, with their respective contributions to overall task success quantified in Table VI. The ablation results reveal clear causal links between modules and task families.

RIK primarily improves reachability robustness. RIK mitigates *no-solution* IK events near singularities or workspace boundaries by relaxing pose tolerances only when strict IK fails. This flexibility is particularly critical for collision-free trajectory tracking (as an example in Fig. 5) and the manipulation of articulated objects. Even in relatively sparse environments, target poses can be geometrically constrained by the volumetric occupancy of obstacles or the kinematic limits of the assembly, yet marginal deviations often remain functionally admissible for maintaining task progress.

CFP primarily improves safety and consistency in clutter. Enabling CFP reduces collision-induced failures by planning in a conservative ESDF derived from single-view RGB-D. The conservative completion of occluded space prevents trajectories from cutting through unobserved cavities, which is a common source of unexpected contacts during approach and placement.

FDR primarily improves long-horizon success by preventing error accumulation. When a step fails (e.g., grasp slips or an object is displaced), the AOG-driven verification and reflection loop updates the SOSG and triggers local repair or replanning. This converts would-be terminal failures into recoverable states, explaining the large gain from V2 to V3 in multi-step tasks such as trash sorting and breakfast preparation.

Overall, these results show that strong long-horizon performance arises from combining grounded state representations and verification-driven recovery with reliable, safety-aware motion generation, rather than relying solely on open-loop

action execution.

E. Mobile Manipulation in Office Environments

To demonstrate the versatility and generalizability of the UniManip framework, we extend its application to a mobile manipulator embodiment as revealed. In this setup, a mobile base equipped with a Realman RM65 robotic arm, as illustrated in Fig. 8, is utilized to perform mobile manipulation tasks from randomly selected docking points within an office environment. The UniManip system employs a Mapless Reactive Navigation strategy, bypassing the computational overhead of global 3D scene reconstruction. This process is governed by the AOG, which instantiates navigation parameters, specifically the target entity O_{target} and the desired docking clearance d_{goal} , as shown in the last *available tool* in Fig. 2, based on high-level task semantics. For perception, we integrate YOLOE [47] as a real-time, open-vocabulary detector to identify the target’s 2D bounding box in the RGB stream. By projecting the filtered point cloud from the eye-in-hand depth sensor onto the detected region, the system estimates the object’s relative centroid in the camera frame.

Navigation is formulated as a Visual Servoing task. To minimize the displacement error, the mobile base executes a dual-loop control law: an angular controller regulates the yaw velocity ω_z to maintain the target within the camera’s principal axis (azimuth alignment), while a linear controller modulates the forward velocity v_x to converge toward the specified docking distance. The control law for the docking phase is defined as:

$$\begin{cases} v_x = K_p \cdot (z_{c,obj} - d_{goal}) \\ \omega_z = K_\theta \cdot \text{atan}2(x_{c,obj}, z_{c,obj}) \end{cases} \quad (23)$$

where $z_{c,obj}$ and $x_{c,obj}$ represent the depth and lateral offset of the object in the camera frame, and $K_p = 0.6$, $K_\theta = 0.2$ are the proportional gains tuned for smooth convergence. This approach ensures that the mobile manipulator reaches an optimal configuration for subsequent manipulation, effectively extending the robot’s reachable workspace without requiring a pre-defined global map.

The experimental setup involves the robot navigating to different docking points, identifying target objects using the perception module, and executing manipulation tasks such as picking and placing items into designated containers. UniManip achieves hardware-agnostic versatility by adapting its IK and planning primitives to varying robot morphologies, effectively integrating the mobile base’s degrees of freedom to facilitate mobile, long-horizon manipulation. This extension showcases the framework’s adaptability and effectiveness in more complex, real-world scenarios where mobility is demanded.

During the mobile manipulation experiments, as shown in Fig. 11, the robot successfully navigated to designated docking points and executed a series of manipulation tasks. At the first docking point, which featured two chairs and a table, the robot prepared breakfast by picking up a banana and a fruit, placing them onto a plate and slicing bread on the table, respectively. Subsequently, the robot moved to a second docking point with

TABLE VI: **Ablation Results.** Success rates (%) across different manipulation categories. The configurations V1, V2, and V3 are defined in Table V.

Category	Task	Objects	Variants of UniManip		
			V1	V2	V3
Rigid obj. manipulation	Sort trash to different container	Plastic bottle, batteries	50	40	90
	Insert bricks	Green Ring, Cube, Base with poles	40	45	70
	Insert rod-shaped object	Eggplant, banana	50	40	80
	Pour water	Bottle, bowl	20	10	60
Deformable obj. manipulation	Prepare breakfast	Bread, apple, banana, plate, bowl	60	40	90
	Sort breads into different plates	Bread roll, loaf of bread, coconut bread	40	50	70
Articulated obj. manipulation	Press a button	Green cylinder	90	90	100
	Open the drawer	Cabinet with opened drawer	60	80	80
	Close the drawer	Cabinet with closed drawer	60	60	70
Average Success Rate across the 90 Trials			52.22	50.56	80.00

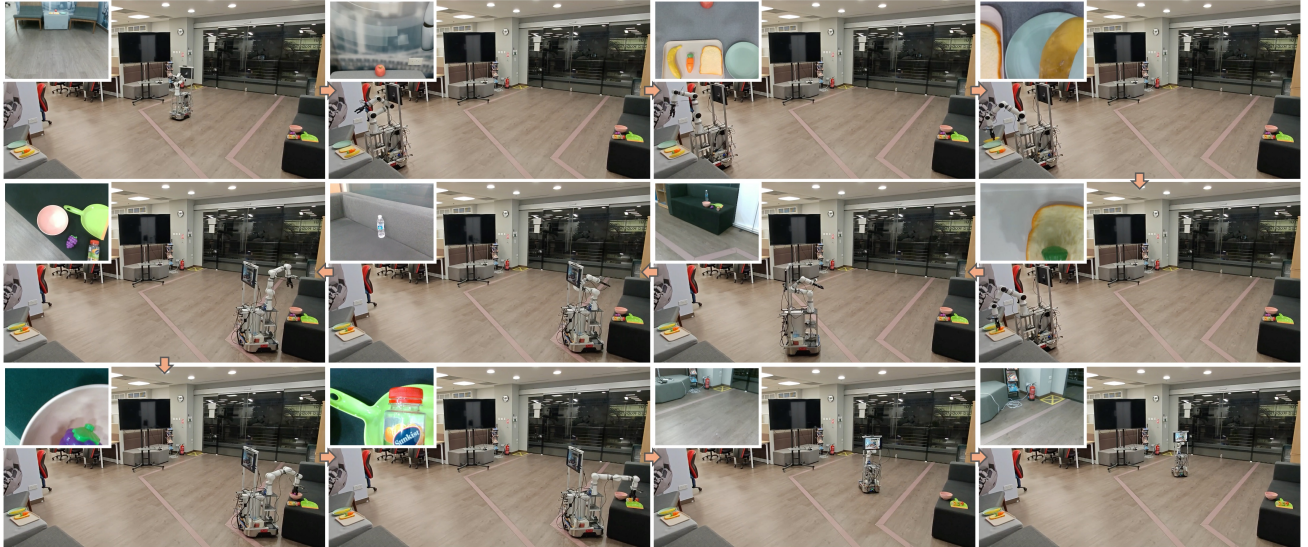


Fig. 11: Demonstration of UniManip framework applied to a mobile manipulation scenario using a mobile base equipped with Realman RM65 robotic arm. The robot navigates to different docking points within an office environment to perform various manipulation tasks.

a bench, where it picked up a grape and an orange juice bottle, placing them into a bowl and a garbage scoop, respectively. The above mobile manipulation experiments revealed two primary technical challenges. First, the introduction of a mobile base coupled the manipulator’s reachability with base stability, requiring the mobile basis to dock for arm extension while maintaining the system’s center of mass within safe margins. Second, varying docking positions introduced significant viewpoint variance. To mitigate these issues, we leveraged an eye-in-hand camera configuration. Unlike traditional eye-to-hand (static external) setups, the end-effector-mounted camera provided a workspace-consistent, high-resolution view that ensured robust object recognition despite the changing base coordinates. This perceptual consistency enabled UniManip to maintain excellent performance across diverse docking scenarios, validating its robustness and adaptability in cross-embodiment and mobile applications.

F. Failure Analysis

To understand the remaining limitations of our proposed framework, we categorize the failure modes observed across evaluation trials (Fig. 12), noting that these instances typically

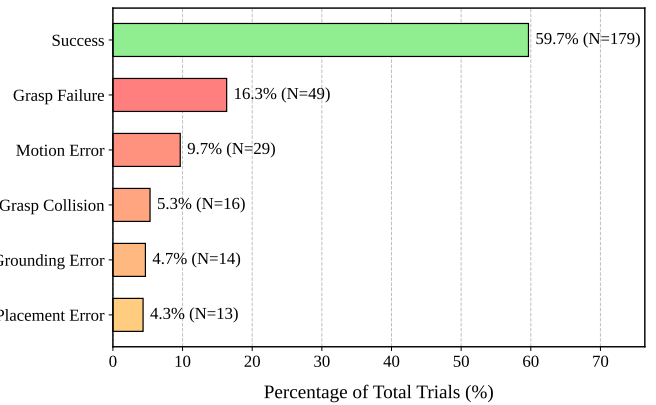


Fig. 12: Breakdown of failure modes observed across all evaluation trials. The chart illustrates the distribution of error types, highlighting that physical interaction failures and kinematic constraints constitute the primary bottlenecks, while semantic grounding remains relatively robust.

stem from operational errors in the execution flow rather than deficiencies in the system’s underlying performance limits. The system achieved a 59.7% overall success rate on the most challenging long-horizon and dexterous tasks, while the remaining 40.3% failures are grouped into categories before any

recovery actions are applied. This isolates intrinsic bottlenecks of the primary perception–planning–execution pipeline, and clarifies where the AOG-based reflection mechanism provides the most leverage.

Physical Interaction Failures (Grasp Failure: 16.3%, Placement Error: 4.3%): The most predominant failure mode is *Grasp Failure*, accounting for 16.3% of all trials. These failures primarily stem from the limitations of single-view depth estimation. When dealing with transparent or reflective objects (e.g., plastic bottles), the depth sensor occasionally generates noisy point clouds, leading to inaccurate gripper pose estimation relative to the object’s center of mass. Similarly, *Placement Errors* (4.3%) often occurred during the release phase, where unstable contact dynamics caused objects to topple upon placement. These physical interaction issues highlight the inherent difficulty of open-loop execution in unmodeled dynamics.

Kinematic and Planning Deviations (Motion Error: 9.7%, Grasp Collision: 5.3%): *Motion Errors* accounted for 9.7% of failures. In the context of mobile manipulation, these were largely caused by the coupling errors between the mobile base and the manipulator. If the base navigation stopped slightly outside the optimal workspace, the arm occasionally encountered kinematic singularities or failed to find a valid IK solution for the requested atomic operation. *Grasp Collisions* (5.3%) typically occurred in dense environments where the gripper fingers made unintended contact with adjacent obstacles during the approach phase, suggesting a need for more conservative safety margins in the low-level trajectory planner.

Semantic Grounding Stability (Grounding Error: 4.7%): Notably, *Grounding Errors* constituted only 4.7% of the total cases. This low error rate is a significant validation of the proposed Bi-level AOG. Despite the complexity of free-form human commands, the Semantic-Operational State Layer successfully filtered the majority of ambiguity, ensuring that the correct object was targeted. The few instances of grounding failure occurred when the VLM misidentified visually similar objects in close proximity or failed to resolve ambiguous spatial descriptions (e.g., distinguishing between *cup* and *mug*).

The Necessity of Reflection: This distribution underscores the motivation behind UniManip’s reflective recovery mechanism. Since 30% of failures (Grasp, Motion, and Placement errors) are execution-based rather than semantic, a static planner would simply fail. By detecting these physical mismatches and triggering the reflection module, UniManip can adjust the docking distance or re-grasp strategy to recover, thereby bridging the gap between perception and successful execution.

VI. CONCLUSION

UniManip provides a general-purpose, zero-shot robotic manipulation framework that tightly couples high-level semantic reasoning with low-level geometric execution via a Bi-level AOG. By grounding free-form commands into an object-centric SOSG and closing the loop with verification, reflection, and recovery, the system remains robust to open-world variations and execution deviations. Experiments demonstrate consistent gains over both end-to-end VLA baselines and

hierarchical open-vocabulary planners. UniManip achieves an average success rate of 93.75% on the VLA benchmark (vs. 71.25% for the strongest baseline) while substantially reducing distractor grasps, and reaches 82.5% task success in cluttered scenes compared with ReKep, MOKA, and VoxPoser. On long-horizon and interaction-rich tasks, the full system attains 80% average success over 90 trials in our ablation suite, highlighting the complementary roles of collision-free planning, relaxed IK, and AOG-driven recovery. Remaining failures are dominated by physical interaction uncertainty and embodiment-dependent kinematic constraints (e.g., grasp instability under single-view depth noise). Future work will focus on improving contact robustness and state estimation (e.g., tactile sensing and uncertainty-aware reconstruction), strengthening embodiment-aware whole-body planning for mobile manipulation, and scaling the agentic memory/recovery mechanism to broader task libraries and multi-robot settings.

REFERENCES

- [1] A. Billard and D. Kragic, “Trends and challenges in robot manipulation,” *Science*, vol. 364, no. 6446, p. eaat8414, 2019.
- [2] Y. Zhang, M. Yin, W. Bi, H. Yan, S. Bian, C.-H. Zhang, and C. Hua, “ZISVFM: Zero-shot object instance segmentation in indoor robotic environments with vision foundation models,” *IEEE Transactions on Robotics*, 2025.
- [3] M. Abou Ali, F. Dornaika, and J. Charafeddine, “Agentic AI: a comprehensive survey of architectures, applications, and future directions,” *Artificial Intelligence Review*, vol. 59, no. 1, p. 11, 2025.
- [4] Y. Guo, Y. Ni, J. Jin, Y. Jiang, D. Li, H. Zhao, and Y. Shen, “Embodied assistant: Robot mobility operations guided by open vocabulary in open environments utilizing ILM,” *IEEE Internet of Things Journal*, 2025.
- [5] B. Zitkovich, T. Yu, S. Xu, P. Xu, T. Xiao, F. Xia, J. Wu, P. Wohlhart, S. Welker, A. Wahid, *et al.*, “RT-2: Vision-language-action models transfer web knowledge to robotic control,” in *Conference on Robot Learning*, pp. 2165–2183, PMLR, 2023.
- [6] M. J. Kim, K. Pertsch, S. Karamcheti, T. Xiao, A. Balakrishna, S. Nair, R. Rafailov, E. P. Foster, P. R. Sanketi, Q. Vuong, *et al.*, “OpenVLA: An open-source vision-language-action model,” in *Conference on Robot Learning*, pp. 2679–2713, PMLR, 2025.
- [7] K. Black, N. Brown, D. Driess, A. Esmail, M. Equi, C. Finn, N. Fusai, L. Groom, K. Hausman, B. Ichter, *et al.*, “ π_0 : A vision-language-action flow model for general robot control,” *arXiv preprint arXiv:2410.24164*, 2024.
- [8] C.-Y. Hung, N. Majumder, H. Deng, L. Renhang, Y. Ang, A. Zadeh, C. Li, D. Herremans, Z. Wang, and S. Poria, “NORA-1.5: A vision-language-action model trained using world model-and action-based preference rewards,” *arXiv preprint arXiv:2511.14659*, 2025.
- [9] A. Amin, R. Aniceto, A. Balakrishna, K. Black, K. Conley, G. Connors, J. Darpinian, K. Dhabalia, J. DiCarlo, D. Driess, *et al.*, “ $\pi_{0.6}^*$: a VLA that learns from experience,” *arXiv preprint arXiv:2511.14759*, 2025.
- [10] W. Huang, C. Wang, Y. Li, R. Zhang, and F.-F. Li, “ReKep: Spatio-temporal reasoning of relational keypoint constraints for robotic manipulation,” in *Conference on Robot Learning*, pp. 4573–4602, PMLR, 2025.
- [11] W. Huang, C. Wang, R. Zhang, Y. Li, J. Wu, and F.-F. Li, “VoxPoser: Composable 3D value maps for robotic manipulation with language models,” in *Conference on Robot Learning*, pp. 540–562, PMLR, 2023.
- [12] H. Liu, S. Guo, P. Mai, J. Cao, H. Li, and J. Ma, “RoboDexVLM: Visual language model-enabled task planning and motion control for dexterous robot manipulation,” *arXiv preprint arXiv:2503.01616*, 2025.
- [13] J.-B. Alayrac, J. Donahue, P. Luc, A. Miech, I. Barr, Y. Hasson, K. Lenc, A. Mensch, K. Millican, M. Reynolds, *et al.*, “Flamingo: a visual language model for few-shot learning,” *Advances in Neural Information Processing Systems*, vol. 35, pp. 23716–23736, 2022.
- [14] H. Chen, J. Liu, C. Gu, Z. Liu, R. Zhang, X. Li, X. He, Y. Guo, C.-W. Fu, S. Zhang, *et al.*, “Fast-in-slow: A dual-system vla model unifying fast manipulation within slow reasoning,” in *The Thirty-ninth Annual Conference on Neural Information Processing Systems*, 2025.
- [15] Z. Jiao, Y. Niu, Z. Zhang, Y. Wu, Y. Su, Y. Zhu, H. Liu, and S.-C. Zhu, “Integration of robot and scene kinematics for sequential mobile manipulation planning,” *IEEE Transactions on Robotics*, 2025.

[16] R. Zhao, T. Ingebrand, S. Chinchali, and U. Topcu, “MoS-VLA: A vision-language-action model with one-shot skill adaptation,” *arXiv preprint arXiv:2510.16617*, 2025.

[17] K. Dreczkowski, P. Vitiello, V. Vosylius, and E. Johns, “Learning a thousand tasks in a day,” *Science Robotics*, vol. 10, no. 108, p. eadv7594, 2025.

[18] P. Li, Y. Wu, Z. Xi, W. Li, Y. Huang, Z. Zhang, Y. Chen, J. Wang, S.-C. Zhu, T. Liu, *et al.*, “ControlVLA: Few-shot object-centric adaptation for pre-trained vision-language-action models,” *arXiv preprint arXiv:2506.16211*, 2025.

[19] M. S. Humphreys, J. D. Bain, and R. Pike, “Different ways to cue a coherent memory system: A theory for episodic, semantic, and procedural tasks,” *Psychological Review*, vol. 96, no. 2, p. 208, 1989.

[20] A. O’Neill, A. Rehman, A. Maddukuri, A. Gupta, A. Padalkar, A. Lee, A. Pooley, A. Gupta, A. Mandlekar, A. Jain, *et al.*, “Open-X-Embodiment: Robotic learning datasets and RT-X models,” in *2024 IEEE International Conference on Robotics and Automation (ICRA)*, pp. 6892–6903, IEEE, 2024.

[21] A. Brohan, N. Brown, J. Carbajal, Y. Chebotar, J. Dabis, C. Finn, K. Gopalakrishnan, K. Hausman, A. Herzog, J. Hsu, *et al.*, “RT-1: Robotics transformer for real-world control at scale,” *Robotics: Science and Systems*, 2023.

[22] D. Driess, F. Xia, M. S. Sajjadi, C. Lynch, A. Chowdhery, B. Ichter, A. Wahid, J. Tompson, Q. Vuong, T. Yu, *et al.*, “PaLM-E: an embodied multimodal language model,” in *Proceedings of the 40th International Conference on Machine Learning*, pp. 8469–8488, 2023.

[23] J. Bjorck, F. Castañeda, N. Cherniadev, X. Da, R. Ding, L. Fan, Y. Fang, D. Fox, F. Hu, S. Huang, *et al.*, “GR00T n1: An open foundation model for generalist humanoid robots,” *arXiv preprint arXiv:2503.14734*, 2025.

[24] H. Deng, Z. Wu, H. Liu, W. Guo, Y. Xue, Z. Shan, C. Zhang, B. Jia, Y. Ling, G. Lu, *et al.*, “A survey on reinforcement learning of vision-language-action models for robotic manipulation,” *Authorea Preprints*, 2025.

[25] K. Black, N. Brown, J. Darpinian, K. Dhabalia, D. Driess, A. Esmail, M. R. Equi, C. Finn, N. Fusai, M. Y. Galliker, *et al.*, “ $\pi_{0.5}$: a vision-language-action model with open-world generalization,” in *9th Annual Conference on Robot Learning*, 2025.

[26] Q. Zhao, Y. Lu, M. J. Kim, Z. Fu, Z. Zhang, Y. Wu, Z. Li, Q. Ma, S. Han, C. Finn, *et al.*, “CoT-VLA: Visual chain-of-thought reasoning for vision-language-action models,” in *Proceedings of the Computer Vision and Pattern Recognition Conference*, pp. 1702–1713, 2025.

[27] M. Zawalski, W. Chen, K. Pertsch, O. Mees, C. Finn, and S. Levine, “Robotic control via embodied chain-of-thought reasoning,” in *Conference on Robot Learning*, pp. 3157–3181, PMLR, 2025.

[28] G. Team, A. Ye, B. Wang, C. Ni, G. Huang, G. Zhao, H. Li, J. Li, J. Zhu, L. Feng, *et al.*, “GigaBrain-0: A world model-powered vision-language-action model,” *arXiv preprint arXiv:2510.19430*, 2025.

[29] Y. Li, Y. Deng, J. Zhang, J. Jang, M. Memmel, R. Yu, C. R. Garrett, F. Ramos, D. Fox, A. Li, *et al.*, “Hamster: Hierarchical action models for open-world robot manipulation,” *arXiv preprint arXiv:2502.05485*, 2025.

[30] F. Liu, K. Fang, P. Abbeel, and S. Levine, “MOKA: Open-vocabulary robotic manipulation through mark-based visual prompting,” in *First Workshop on Vision-Language Models for Navigation and Manipulation at ICRA*, 2024.

[31] H. Huang, F. Lin, Y. Hu, S. Wang, and Y. Gao, “CoPa: General robotic manipulation through spatial constraints of parts with foundation models,” in *2024 IEEE/RSJ International Conference on Intelligent Robots and Systems (IROS)*, pp. 9488–9495, IEEE, 2024.

[32] M. Pan, J. Zhang, T. Wu, Y. Zhao, W. Gao, and H. Dong, “OmniManip: Towards general robotic manipulation via object-centric interaction primitives as spatial constraints,” in *Proceedings of the Computer Vision and Pattern Recognition Conference*, pp. 17359–17369, 2025.

[33] Y. Li, X. Ma, J. Xu, Y. Cui, Z. Cui, Z. Han, L. Huang, T. Kong, Y. Liu, H. Niu, *et al.*, “GR-RL: Going dexterous and precise for long-horizon robotic manipulation,” *arXiv preprint arXiv:2512.01801*, 2025.

[34] B. Wu, F. Xu, Z. He, A. Gupta, and P. K. Allen, “Squirl: Robust and efficient learning from video demonstration of long-horizon robotic manipulation tasks,” in *2020 IEEE/RSJ International Conference on Intelligent Robots and Systems (IROS)*, pp. 9720–9727, IEEE, 2020.

[35] A. C. Ak, E. E. Aksoy, and S. Sariel, “Learning failure prevention skills for safe robot manipulation,” *IEEE Robotics and Automation Letters*, vol. 8, no. 12, pp. 7994–8001, 2023.

[36] S. Vats, D. K. Jha, M. Likhachev, O. Kroemer, and D. Romero, “RecoveryChaining: Learning local recovery policies for robust manipulation,” in *2025 IEEE/RSJ International Conference on Intelligent Robots and Systems (IROS)*, pp. 9776–9783, IEEE, 2025.

[37] A. Inceoglu, E. E. Aksoy, and S. Sariel, “Multimodal detection and classification of robot manipulation failures,” *IEEE Robotics and Automation Letters*, vol. 9, no. 2, pp. 1396–1403, 2023.

[38] S. Parastegari, E. Noohi, B. Abbasi, and M. Žefran, “Failure recovery in robot–human object handover,” *IEEE Transactions on Robotics*, vol. 34, no. 3, pp. 660–673, 2018.

[39] H. Singh, R. J. Das, M. Han, P. Nakov, and I. Laptev, “MALMM: Multi-agent large language models for zero-shot robotic manipulation,” in *2025 IEEE/RSJ International Conference on Intelligent Robots and Systems (IROS)*, pp. 20386–20393, IEEE, 2025.

[40] S. Liu, Z. Zeng, T. Ren, F. Li, H. Zhang, J. Yang, Q. Jiang, C. Li, J. Yang, H. Su, *et al.*, “Grounding DINO: Marrying DINO with grounded pre-training for open-set object detection,” in *European Conference on Computer Vision*, pp. 38–55, 2024.

[41] N. Ravi, V. Gabeur, Y.-T. Hu, R. Hu, C. Ryali, T. Ma, H. Khedr, R. Rädel, C. Rolland, L. Gustafson, E. Mintun, J. Pan, K. V. Alwala, N. Carion, C.-Y. Wu, R. Girshick, P. Dollar, and C. Feichtenhofer, “SAM 2: Segment anything in images and videos,” in *The 13th International Conference on Learning Representations*, 2025.

[42] R. L. Carneiro and R. G. Perrin, “Herbert spencer’s principles of sociology: A centennial retrospective and appraisal,” *Annals of Science*, vol. 59, no. 3, pp. 221–261, 2002.

[43] H. Liu, K. Chen, Y. Li, Z. Huang, M. Liu, and J. Ma, “UDMC: Unified decision-making and control framework for urban autonomous driving with motion prediction of traffic participants,” *IEEE Transactions on Intelligent Transportation Systems*, vol. 26, no. 5, pp. 5856–5871, 2025.

[44] K. Shoemake, “Animating rotation with quaternion curves,” in *Proceedings of the 12th Annual Conference on Computer Graphics and Interactive Techniques*, pp. 245–254, 1985.

[45] C.-Y. Hung, Q. Sun, P. Hong, A. Zadeh, C. Li, U. Tan, N. Majumder, S. Poria, *et al.*, “NORA: A small open-sourced generalist vision language action model for embodied tasks,” *arXiv preprint arXiv:2504.19854*, 2025.

[46] A. Yang, A. Li, B. Yang, B. Zhang, B. Hui, B. Zheng, B. Yu, C. Gao, C. Huang, C. Lv, *et al.*, “Qwen3 technical report,” *arXiv preprint arXiv:2505.09388*, 2025.

[47] A. Wang, L. Liu, H. Chen, Z. Lin, J. Han, and G. Ding, “YOLOE: Real-time seeing anything,” *arXiv preprint arXiv:2503.07465*, 2025.